Applied Thermal Engineering 200 (2022) 117640

Contents lists available at ScienceDirect

Applied Thermal Engineering

journal homepage: www.elsevier.com/locate/apthermeng

Optimization design of helical micro fin tubes based on exergy destruction minimization principle

J.H. Xie, H.C. Cui, Z.C. Liu, W. Liu *

School of Energy and Power Engineering, Huazhong University of Science and Technology, Wuhan 430074, China

ARTICLE INFO

Keywords:
Helical micro fin tubes
Geometrical parameters optimization
Exergy destruction minimization principle
Artificial neural network
Genetic algorithm

ABSTRACT

The helical micro fin tubes (HFT) are commonly used in various double pipe heat exchangers because of the excellent processing and anti-fouling performance. It is of great significance to further improve the overall efficiency of the HFT so as to diminish energy consumption. In this work, the heat transfer and flow characteristics of the HFT are studied by numerical simulation. The results show that the heat transfer enhancement factors of the HFT are the secondary flow generated near the wall and the increase of the heat exchange area. In addition, the effects of the geometrical parameters on thermal–hydraulic performance are studied at $Re = 36{,}636$. It is found that the micro fin height (e), the helical angle (φ), and the number of starts (Ns) have a significant impact on the overall performance, and there is a strong mutual coupling between them. According to the parametric analysis, the HFT with a low micro fin height and a large number of starts is considered to be a better geometrical type. Finally, in order to select (or design) the HFT quickly under the specific working conditions, based on the exergy destruction minimization principle, the geometrical parameters are optimized by using the artificial neural network and genetic algorithm. An optimal solution ($e = 0.23$ mm, $\varphi = 36.1°$, and $Ns = 66$) is selected from the Pareto front by the TOPSIS method. The results indicate that the optimal solution has a sensible balance between the exergy destruction caused by heat transfer and fluid flow. Besides, it has a better thermal–hydraulic performance as well ($PEC = 1.73$). This work fills the gap of heat transfer and the geometrical optimization study of HFT based on the second law of thermodynamics and provides strong evidence that the exergy destruction minimization principle is still applicable in the case of the periodic model and fully developed turbulence. We hope that it will be contributed to the structural design of the HFT.

1. Introduction

Heat exchangers are widely used in electric power, petrochemical, metallurgy, machinery manufacturing, and other industrial fields. Improving the overall performance of heat exchangers is of great significance for industrial energy utilization efficiency and diminishing energy use. The overall performance of heat exchangers is determined by the heat transfer efficiency of the heat transfer tubes, which are the primary heat transfer units for a heat exchanger. Thus, it is necessary to develop efficient enhanced heat transfer tubes in practical applications. In the past few decades, researchers have conducted in-depth researches on the heat transfer process inside the tubes and developed a variety of heat transfer enhancement tubes with high efficiency such as the corrugated tubes [1,2], dimples tubes [3], spirally grooved tubes [4,5], and tube inserts [6,7]. A comprehensive literature review of these tubes had been conducted by Ji et al. [8]. In particular, the helical micro fin tubes (HFT) are commonly used in various shell and tube heat exchangers due to the excellent processing and anti-fouling performance. Owing to the extensive use of these heat exchange equipment, any slight performance improvement of the HFT will yield substantial economic benefits.

Many researchers have conducted a lot of experiments on the HFT [9–11] and measured the thermal–hydraulic performance with different geometrical parameters. These experiments aimed to study the relationship between the heat transfer and friction characteristics and build the empirical correlation between the Nusselt number (or friction factor) and the geometrical parameters. However, the empirical correlations proposed by different researchers were affected by many factors such as the experimental methods, measuring instruments, and data processing methods. As a result, these correlations may be used in a limited range of geometrical parameters or working conditions. In contrast, the numerical simulations, which can provide detailed flow specialties and temperature distributions, contribute to the investigation of the heat

* Corresponding author.
E-mail address: w_liu@hust.edu.cn (W. Liu).

https://doi.org/10.1016/j.applthermaleng.2021.117640
Received 11 May 2021; Received in revised form 24 August 2021; Accepted 30 September 2021
Available online 7 October 2021

Nomenclature

b	bias of ANN
c_p	pecific heat at constant pressure,J/(kg·K)
$C_{1\varepsilon}$, $C_{2\varepsilon}$	constants for turbulence model
D_o, D_i	outer and inner diameters of the tube,mm
e	micro fin height,mm
$E_{xd,\Delta T}$	thermal dissipation,W/m^3
$E_{xd,\Delta p}$	power consumption,W/m^3
f	fanning friction factor
h	average equivalent heat transfer coefficient,W/(m^2·K)
J_1	thermal dissipation reduction rate
J_2	power consumption increasing rate
m	number of neurons in the hidden layer
$\dot{m}$	mass flow rate,kg/s
MSE	root mean square error
n	number of minimum repeating units
Ns	number of starts
Nu	Nusselt number
p	pressure,Pa
$\frac{dp}{dl}$	unit pressure drop,Pa/m
P	micro fin pitch,mm
PEC	overall performance
q	heat flux,W/m^2
R^2	regression coefficient
Re	Reynolds number
S, $S_{i,j}$	rotation rate tensor,m/s
S_{gen}	entropy generation,W/(m^3·K)
t_t, t_b	top and base widths of the micro fin,mm
T	temperature,K
T_0	ambient temperature,K
w	weight of ANN

Greek symbols

ε	turbulence dissipation rate,m^2/s^3
κ	turbulence kinetic energy,m^2/s^2
λ	thermal conductivity,W/(m·K)
μ	dynamic viscosity,Pa·s
μ_t	eddy viscosity coefficient
ρ	density,kg/m^3
σ_κ, σ_ε	turbulent Prandtl numbers for κ andε
φ	helical angle, °
ω	specific dissipation rate,1/s

Subscript

0	smooth tube
ANN	artificial neural network
i, j, k	input, hidden, and output layer, respectively

transfer enhancement mechanism and the characteristics of the internal convective heat transfer process. In conclusion, numerical simulations can be used as the complement to experiments while providing the direction of the heat transfer enhancement for the HFT.

As mentioned, in order to select or design the HFT quickly, the numerical investigation will be a better choice, resulting from its convenience, low cost, and time-saving. Many studies [12–15] have demonstrated that the Nusselt number and friction factor predicted by the appropriate turbulence model present a slight deviation from the experimental data. Therefore, it is considered that the numerical investigation method is appropriate and effective. Li et al. [13] numerically investigated the influence of the geometrical parameters on the thermal–hydraulic performance of the HFT. Their results indicated that the ratio of the pitch to micro fin height affected the separation and the mixing of the boundary layer near the wall. Besides, the range of the optimal geometrical parameters (0.3–0.6 mm for the micro fin height, 25–35° for the helical angle, and 40–50 for the number of starts) was found for the HFT (15.54 mm for the inner diameter) when the Reynolds number equals 27,000 by the parametric analysis method. However, due to the strong mutual coupling between the various parameters, this method can determine the approximate optimal range interval rather than the precise value. Therefore, it is necessary to apply professional optimization algorithms instead of traditional parametric studies for geometrical parameters optimization.

In recent years, in the field of heat transfer optimization, the method of using professional optimization algorithms to obtain the optimal solution has been adopted by many researchers. Hamed et al. [16] achieved a multi-objective optimization of turbulent heat transfer flow in helically corrugated tubes by using NSGA-II algorithm. In work of Hossein et al [17], the single and multi-objective BAHPSO are investigated for thermal designing of the cross-flow plate fin heat exchanger under given heat duty and pressure drop constraints. Ocłoń et al. [18] used particle swarm optimization methods and continuous genetic algorithms to optimize manifold shape in the high temperature finned-tube heat exchangers. Their design enlarged the volume of the fluid and improved the flow distribution to tubular space of heat exchanger. Bashir et al. [19] developed a new Genetic Algorithm (GA) based to combined with Computational Fluid Dynamics (CFD) to produce optimized fin shapes for heat exchangers used in aerospace applications. As for the HFT, Dastmalchi et al. [14] used the particle swarm algorithm to optimize micro fin height, the helical angle, and the number of starts based on the increasing rate of the heat transfer coefficient and friction factor. The results indicated that when the Reynolds number was in the range of 3×10^3–10^5, the optimal number of starts was around 60. And the optimal values of the helical angle and micro fin height could be roughly calculated by the equations. Garrett et al. [15] performed a multi-objective optimization to obtain the 2D helical micro fin surface of the HFT when the Reynolds number was 49,013. The micro fin height, helical angle, and the number of starts were varied to find the Pareto front of two objectives (minimum friction enhancement and maximum heat transfer enhancement) in their work. In addition, they found that at higher enhancement levels, especially for the helical angle greater than 45°, there was a consistent double vortex between the micro fins, and the relationship between heat transfer enhancement and geometry was chaotic rather than smooth.

As mentioned above, most studies focus on the heat transfer and the power consumed in the convective heat transfer process inside the HFT, which is based on the first law of thermodynamics. In fact, the convective heat transfer process needs to consider not only the heat transfer quantity but also the heat transfer quality. In other words, the irreversible loss should be considered in the optimization of convective heat transfer. Some scholars have proposed the heat transfer optimization principle based on the second law of thermodynamics, such as the entropy generation minimization principle proposed by Bejan et al. [20,21], the entransy dissipation extreme optimization principle proposed by Guo et al. [22], and exergy destruction minimization principle proposed by Liu et al. [23]. In particular, different from the others, the exergy destruction minimization principle comprehensively considers the irreversibility caused by heat transfer and fluid flow in the convective heat transfer process. Moreover, the exergy efficiency representing the utilization efficiency of the input exergy was put forward [24]. These studies have demonstrated the fact that the exergy destruction minimization principle is an effective method for convective heat transfer optimization.

To sum up, most published literature investigated the heat transfer and flow characteristics of the HFT based on the first law of thermodynamics. Furthermore, little research paid attention to the irreversibility of the convective heat transfer process inside the HFT. Thus, in this paper, in addition to the research on thermal–hydraulic performance, the effects of geometrical parameters on exergy destruction are studied as well based on the second law of thermodynamics. Besides, to achieve the best performance and guide actual production and manufacturing, multi-objective optimization of the geometrical parameters is carried out based on the exergy destruction minimization principle, coupled with the artificial neural network and genetic algorithm. This work fills the gap of heat transfer and the geometrical optimization study of the helical micro fin tubes based on the second law of thermodynamics. On the other hand, it provides strong evidence that the exergy destruction minimization principle is still applicable in the case of the periodic model and fully developed turbulence, which was lacking in previous literature.

2. Material and methods

2.1. Geometrical model

Since this study mainly focuses on the convective heat transfer process inside the HFT, as shown in Fig. 1, to save computing resources, the physical model is established by SpaceClaim software after simplifying the external micro fins. Copper is chosen as the base material. The outer diameter (D_o) and inner diameter (D_i) of the tube are 18.8 mm and 15.6 mm, respectively. The top width (t_t) and base width (t_b) of the micro fin are 0.2 mm and 0.3 mm, respectively. The micro fin pitches (P) are given by Eq. (1). Particularly, the tube section surrounded by two adjacent completely overlapping end surfaces is called the minimum repeating unit of the HFT. This paper selects 4 repeating units for modeling.

$$P = \frac{\pi D_i}{Nstan\varphi} \tag{1}$$

The research results of Liu et al. [25] indicated that the shape of the micro fins has minor effects on the thermal–hydraulic performance of the entire tube. On the contrary, the performance is mainly affected by the micro fin height (e), helical angle (φ), and the number of starts (Ns). Referring to the results of the previous geometrical parameters optimization for the HFT [13–15,26], the range of geometrical parameters is 0.2 mm $\le e \le$ 0.6 mm, 20° $\le \varphi \le$ 60°, and 30 $\le Ns \le$ 70.

2.2. Governing equations and boundary conditions

To simplify the numerical simulation, several assumptions are made as follows:

(1) The turbulent flow inside the tube is three-dimensional and steady-state;
(2) The effects of gravity, environmental heat leakage, and viscous dissipation are ignored;
(3) The fluid domain working medium (water) and the solid domain material (copper) have constant physical properties.

Based on the assumptions above, the governing equation in the solid domain is introduced as:

$$\frac{\partial}{\partial x_i}\left(\lambda_s \frac{\partial T}{\partial x_i}\right) = 0 \tag{2}$$

where $\lambda_s = 387.6$ W/(m·K).

The governing equations in the fluid domain are given as follows.

Continuity equation:

$$\frac{\partial(\rho u_i)}{\partial x_i} = 0 \tag{3}$$

Momentum equation:

$$\frac{\partial(\rho u_i u_j)}{\partial x_i} = -\frac{\partial p}{\partial x_j} + \frac{\partial}{\partial x_i}\left(\mu \frac{\partial u_j}{\partial x_i}\right) \tag{4}$$

Energy equation:

$$\frac{\partial(u_i T)}{\partial x_i} = \frac{\partial}{\partial \mathrm{x_i}}\left(\frac{\lambda}{\rho c_p}\frac{\partial \mathrm{T}}{\partial \mathrm{x_i}}\right) \tag{5}$$

Turbulence kinetic energy equation:

$$\frac{\partial}{\partial x_j}(\rho u_j \kappa) = \frac{\partial}{\partial x_j}\left[\left(\mu + \frac{\mu_t}{\sigma_\kappa}\right)\frac{\partial \kappa}{\partial x_j}\right] + 2\mu_t \frac{\partial u_i}{\partial x_j} S_{i,j} - \rho\varepsilon \tag{6}$$

Turbulence energy dissipation equation:

$$\frac{\partial}{\partial x_i}(\rho \mu_i \varepsilon) = \frac{\partial}{\partial x_i}\left[\left(\mu + \frac{\mu_t}{\sigma_\varepsilon}\right)\frac{\partial \varepsilon}{\partial x_i}\right] + C_{1\varepsilon}\rho S\varepsilon - C_{2\varepsilon}\rho \frac{\varepsilon^2}{\kappa + \sqrt{\nu\varepsilon}} \tag{7}$$

where κ and ε are the turbulent kinetic energy and turbulent energy dissipation rate, respectively; σ_κ and σ_ε are the turbulent Prandtl numbers for κ and ε, respectively; $S_{i,j}$ S, $C_{1\varepsilon}$ are given by the following

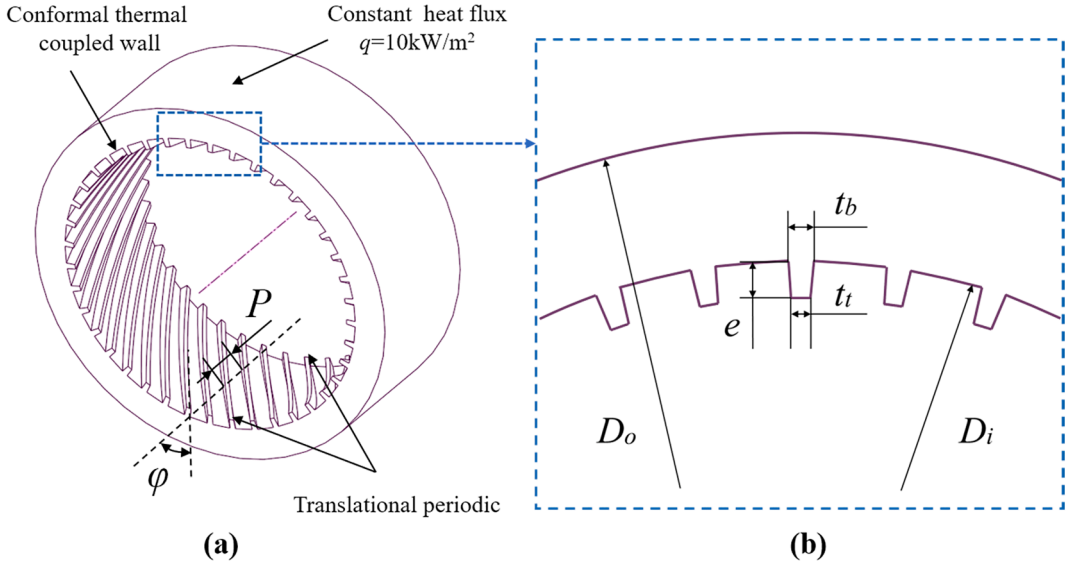

Fig. 1. Geometrical characteristics of the HFT.

equations, where $C_{2\varepsilon}$ equals 1.92.

$$S_{i,j} = \frac{1}{2}\left(\frac{\partial u_i}{\partial x_j} + \frac{\partial u_j}{\partial x_i}\right) \tag{8}$$

$$S = \sqrt{(2S_{i,j}S_{i,j})} \tag{9}$$

$$C_{1\varepsilon} = max\left\{0.43, \frac{\overline{\mu}}{5+\overline{\mu}}\right\} \tag{10}$$

In this study, the translational periodic boundary condition is used to obtain the fully developed flow similar to many simulation studies [27–29]. The domain is solved repeated times as flow over the small region evolves to the fully developed solution. The assumption of periodicity implies that the velocity repeats themselves in space as follows [27]:

$$\boldsymbol{u}(x,y,z) = \boldsymbol{u}(x+L,y,z) = \boldsymbol{u}(x+2L,y,z) = \ldots \tag{11}$$

where L is the periodic length vector of the domain considered.

In contrast to the velocity field, the pressure is not periodic in the sense of Eq. (11). Instead, the pressure drop between modules is periodic. The local pressure gradient can be decomposed into two parts: the gradient of a periodic component, and the gradient of a linearly-varying component. The periodic pressure is the pressure left over after subtracting out the linearly-varying pressure. Pressure drop can be calculated as [30]:

$$\Delta p = p(x,y,z) - p(x+L,y,z) = p(x+L,y,z) - p(x+2L,y,z) = \ldots \tag{12}$$

Similar to pressure periodicity, temperature periodicity for the energy equation is transformed to a dimensionless temperature parameter as proposed by Patankar et al. [31] for a constant wall-temperature boundary condition as described below:

$$\widetilde{\theta}(x,y,z) = \frac{T(x,y,z) - T_{wall}}{T_{bulk,inlet} - T_{wall}}, x \in [0,L] \tag{13}$$

The enhanced wall treatment is adopted in the near-wall region to better capture the flow characteristics. It is a near-wall modeling method that combines a two-layer model with so-called enhanced wall functions [32]. If the near-wall grid is fine enough to be able to resolve the viscous sublayer, then the enhanced wall treatment will be identical to the traditional two-layer zonal model. The two-layer approach is an integral part of the enhanced wall treatment and is used to specify both and the turbulent viscosity in the near-wall cells. In this approach, the whole domain is subdivided into a viscosity-affected region and a fully-turbulent region. The demarcation of the two regions is determined by a wall-distance-based, turbulent Reynolds number, Re_y, defined as:

$$Re_y = \frac{\rho y\sqrt{k}}{\mu} \tag{14}$$

In the fully turbulent region (Re_y greater than 200), the realizable κ-ε model is employed. In the viscosity-affected near-wall region (Re_y ⟨200), the one-equation model of Wolfstein [33] is employed. In the one-equation model, the momentum equations and the κ equation are retained as described.

All the above governing equations are solved by using the Fluent 2019R3 software based on the finite volume method. The translational periodic boundary condition is adopted at the inlet and outlet of the tube section, whose bulk temperature is 300 K and mass flow rate is 0.45 kg/s (Re = 36,636). A constant heat flux (10 kW/m^2) is applied to the outer side of the tube. The inner wall of the tube is a fluid–solid coupled heat transfer wall, and the enhanced wall treatment is used for the near-wall region. The coupled pressure–velocity coupling algorithm is adopted to discretize the governing equations. The second-order upwind scheme is applied for the momentum, energy, turbulent kinetic energy, and turbulent dissipation rate. The convergence criterion is 10^{-6} for the continuity, velocity, and turbulence equation and 10^{-8} for the energy equation.

2.3. Data reduction

Due to the non-uniform distribution of the fluid field, the temperature and pressure of each grid cell will be different. Therefore, the mass average weighted method is adopted to obtain the average temperature and pressure of the fluid, while the area average weighted method for the solid region.

The Reynolds number (Re) based on a round tube mass flow rate is given by:

$$Re = \frac{\rho u_{avg} D_i}{\mu} = \frac{4\dot{m}}{\mu\pi D_i} \tag{15}$$

where u_{avg} is the mean velocity in a smooth tube which has the same inner diameter and mass flow rate; $\dot{m}$ is the mass flow rate.

To reduce the effects of the internal surface area and the micro fins corner area on the further study, the average equivalent heat transfer coefficient (h) is defined based on the outer surface of the tube instead of the strict heat transfer surface. The expression is defined as:

$$h = \frac{q}{T_w - T_f} \tag{16}$$

where q is average heat flux; T_w and T_f are the average temperature of the outer wall and the fluid, respectively.

The Nusselt number (Nu) is defined as:

$$Nu = \frac{hD_i}{\lambda} \tag{17}$$

Correspondingly, the Fanning friction factor (f) can be written as:

$$f = \frac{D_i}{2\rho u_{avg}^2}\frac{dp}{dl} = \frac{\rho\pi^2 D_i^5}{32\dot{m}^2}\frac{dp}{dl} \tag{18}$$

where $\frac{dp}{dl}$ is the unit pressure drop of the flow direction.

To describe the comprehensive performance of the tube, the overall performance (PEC) is defined as:

$$PEC = \frac{Nu/Nu_0}{(f/f_0)^{1/3}} \tag{19}$$

where Nu_0 and f_0 are the Nusselt number and fanning friction factor of the smooth tube at the same working conditions.

According to the exergy destruction minimization principle, the thermal dissipation ($E_{xd,\Delta T}$) and power consumption ($E_{xd,\Delta p}$) can be calculated as follows [23]:

$$E_{xd,\Delta T} = \iiint_{\Omega} T_0 \frac{\lambda(\nabla T)^2}{T^2} \tag{20}$$

$$E_{xd,\Delta p} = \iiint_{\Omega} (\boldsymbol{U}\cdot\nabla p) \tag{21}$$

where T_0 is the ambient temperature; $\boldsymbol{U}$ is the velocity vector.

2.4. Model verification

2.4.1. Grid independence

According to the published literature [34,35], for the numerical simulation of complex geometrical shapes, polyhedral grids have relatively higher calculation accuracy, better convergence, and consume fewer computing resources than tetrahedral grids. Therefore, as shown in Fig. 2, the polyhedral grids are selected to discretize the fluid and solid domains. To better capture the flow characteristics near the wall, several prismatic layers perpendicular to the wall are generated near the inner surface wall. In order to ensure that the y + value meets the requirements [36], the grid height of the first layer and the grid growth

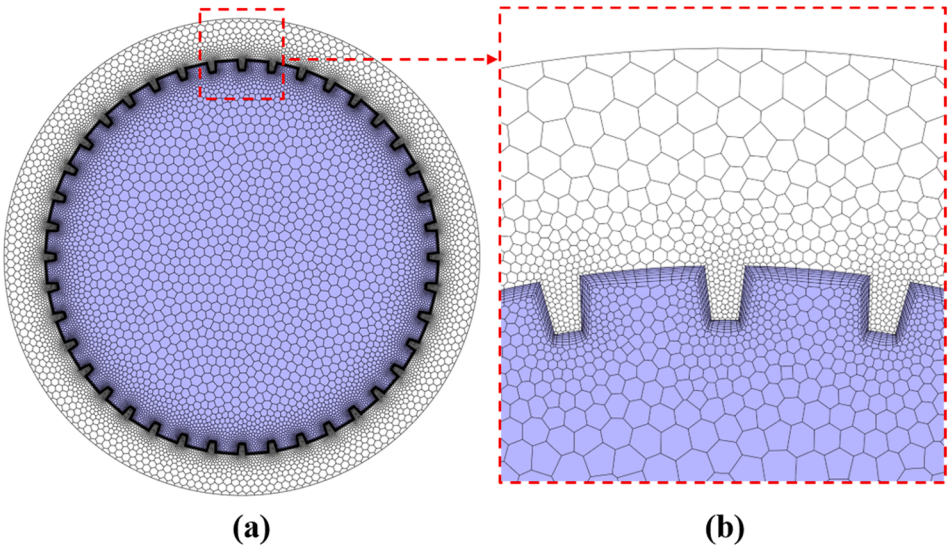

Fig. 2. Grid generation for the computional domain: (a) overall schematic; (b) enlarged view near the wall.

factor are set to 0.01 mm and 1.1, respectively. Furthermore, to minimize the influence of the grids on the calculation results and improve the accuracy of the numerical simulation, different meshing strategies are used to generate three grid systems for the same geometrical model (e = 0.3 mm, $\varphi = 30°$, and $Ns = 30$). The grid convergence index (GCI) [37] method, measuring the deviation percentage of the present numerical value relative to the asymptotic numerical value, is applied to evaluate the grid independent verification results. The results are shown in Table 1. As the grid number increases from 1,730,990 to 3,997,480, the average deviations of Nu and f are 0.058% and 0.148%, respectively. Besides, the GCI values are little, with being 0.25% and 0.24% for Nu and f, respectively. Hence, the grid system of Strategy #2 is dense enough and selected for simulations in this paper.

2.4.2. Turbulence model verification

It is well known that for the numerical simulation, the appropriate turbulence model is crucial to the accuracy of the results. Zoltán et al. [12] compared the accuracy of LES and RANS turbulence models (the κ-ε model and κ-ω model) for predicting heat transfer and fluid flow inside the HFT. The LES model was proven to have the highest accuracy rate, which can better capture the fluid flow characteristics near the wall. However, it will consume much heavy computing resources. Considering the accuracy of the results and the computing resources, the RANS turbulence models are more appropriate for this study. The commonly used RANS turbulence models in engineering applications, including the realizable κ-ε model, the SST κ-ω model, and the Reynolds stress model, are adopted to investigate the steady-state and three-dimensional turbulent flow, heat transfer and fluid flow characteristics.

Webb et al. [9] experimentally measured the heat transfer and flow characteristics of the HFT with a variety of different geometrical parameters. In their experimental procedure, the heat transfer data were taken for cooling of water inside a 2.5 m long double-pipe heat exchanger. Water flowed inside the tube and R12 at a saturation pressure of 517 kPa boiled on the shell side. The R12 vapor was condensed against cold aqueous ethylene glycol in a separate condenser. The average heat flux and refrigerant saturation temperature were held constant during the test. The friction factor was measured for isothermal flow. In this section, experimental data of the tube3 (e = 0.4 mm, $\varphi = 45°$, and $Ns = 30$) are selected to test the accuracy of the turbulence models.

As shown in Fig. 3, the results obtained by these turbulence models are compared with the experimental data. Obviously, the variation trends of the Nusselt number and friction factor with the Reynolds number obtained by different turbulence models are almost same as those in experiments. For the Nusselt number, the values calculated by the realizable κ-ε model and RSM model are relatively accurate, and the average deviations from the experimental data are −8.53% and + 7.38%, respectively. As for the friction factor, the average deviations between the numerical and experimental data of the realizable κ-ε model, SST κ-ω model, and RSM model are −2.98%, −8.4%, and + 39.04%, quantitatively. Therefore, the realizable κ-ε model is employed for the further numerical simulation in the present work.

2.4.3. Periodic boundary verification

Since the lengths of the minimum repeating unit with the different helical angles or the numbers of starts are different, the lengths of the periodic models will be different as well. To clarify whether the different periodic lengths will affect the numerical simulation results, the results of the periodic models with different periodic lengths and the long tube model are compared. Note that the periodic lengths are represented by the number of minimum repeating units (n), and the length of the long tube model is 500 mm. The results of the comparison are shown in Fig. 4. The average deviations of Nu and f calculated by the different periodic lengths models are pretty small, both of which are below 0.1%. In addition, the results of Nu and f calculated by the different periodic lengths models are smaller than the results calculated by the long tube model. The maximum deviations of Nu and f are −6.2% and −4.7%, respectively, both within the acceptable range. In addition, the analysis in section 2.2 displays the small deviation between the numerical simulation results and the experimental data. Therefore, it can be

Table 1
Results of grid independence tests.

Strategy	Grid number	Nu	err,\%	GCI,\%	f	err, \%	GCI, \%
#1	945,394	402.40	0.119	0.36	0.01343	0.519	0.53
#2	1,730,990	402.88	0.058	0.25	0.01350	0.148	0.24
#3	3,997,480	403.11	–	–	0.01352	–	–

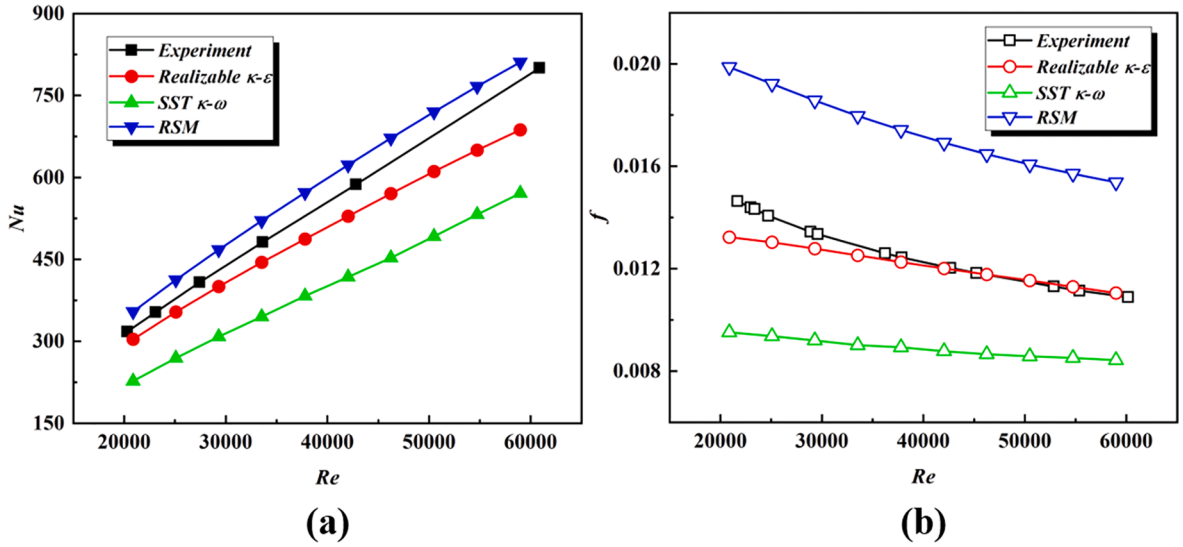

Fig. 3. Validation of turbulence models: (a) Nusselt number; (b) friction factor.

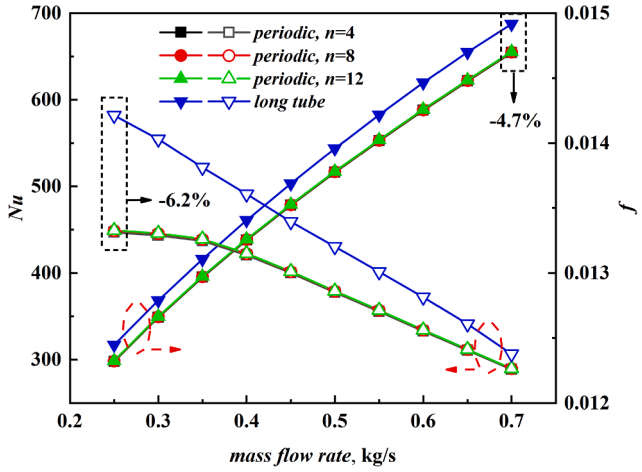

Fig. 4. Results of the different periodic lengths study.

considered that the geometrical model with four repeated units adopted in this work can meet the following calculation requirements.

2.5. Geometric parameter optimization method

2.5.1. Optimization objectives and procedure

The previous parametric analysis indicates that the heat transfer and flow characteristics are greatly affected by the geometrical parameters, and the coupling effect between the parameters is pretty strong. Therefore, it's unreasonable to obtain the optimal structure only based on the parametric analysis. An overall optimization using the professional optimization algorithm will be essential.

It is worth noting that the average thermal dissipation and the average power consumption calculated by Eq. (20) and Eq. (21) have a significant difference in numerical value. In order to reduce the impact of the magnitude difference on the subsequent optimization, it is feasible to construct the dimensionless optimization objectives based on the smooth tube. Therefore, The two optimization objectives are given as follows.

$$J_1 = -\frac{E_{xd,\Delta T,0}}{E_{xd,\Delta T}} \tag{22}$$

$$J_2 = \frac{E_{xd,\Delta p}}{E_{xd,\Delta p,0}} \tag{23}$$

where $E_{xd,\Delta T,0}$ and $E_{xd,\Delta p,0}$ are the average thermal dissipation and average power consumption of the smooth tube, respectively. Considering the heavy workload of the direct optimization by the numerical simulation method, the artificial neural network (ANN) is adopted as the surrogate model to express the relationship between the design variables and optimization objectives. The numerical simulation results are used as the input and output sample data of the ANN, and the ANN fitting data are used as the optimization objective functions. The genetic algorithm (GA) is employed to optimize it. Finally, the optimal solution is selected from the Pareto front according to the appropriate evaluation indicators. The flow chart of the whole process is shown in Fig. 5.

2.5.2. Design of artificial neural networks

As mentioned above, the ANNs are applied to train the recorded data created by the numerical simulations. The three-layer networks with the Tansig transfer function at the hidden layer and the Purelin transfer function at the output layer based on the back propagation algorithm are adopted for these two objectives. The percentages of the training, validation and test sets are set to 70%, 15% and 15%, respectively. It should be noted that the input data need to convert to the suitable form. So, all data are scaled to the range of [0, 1]. And the correlation of scaled J_1 and J_2 can be expressed as [38]:

$$J_1 \text{ or } J_2 = \sum_{j=1}^{m} w_{1j}\left(\frac{2}{1+e^{-2\left(\sum_{i=1}^{3} w_{ji}x_i + b_j\right)} - 1}\right) + b_k \tag{24}$$

where w is the weight; m is the number of neurons in the hidden layer; the subscript i, j and k refer to the input, hidden, and output layer, respectively.

Two evaluation indicators (root mean square error *MSE*, regression coefficient R^2) widely used in the statistics field are employed to evaluate the ANNs [38]. They are defined as Eq. (25) and Eq. (26). The smaller *MSE* is and the larger R^2 is, the higher the accuracy will be and the better performance the ANN will have.

$$MSE = \frac{1}{N}\sum_{i=1}^{N}\left(x_{i,ANN} - x_i\right)^2 \tag{25}$$

$$R^2 = 1 - \sum_{i=1}^{N}\frac{\left(x_{i,ANN} - x_i\right)^2}{x_i^2} \tag{26}$$

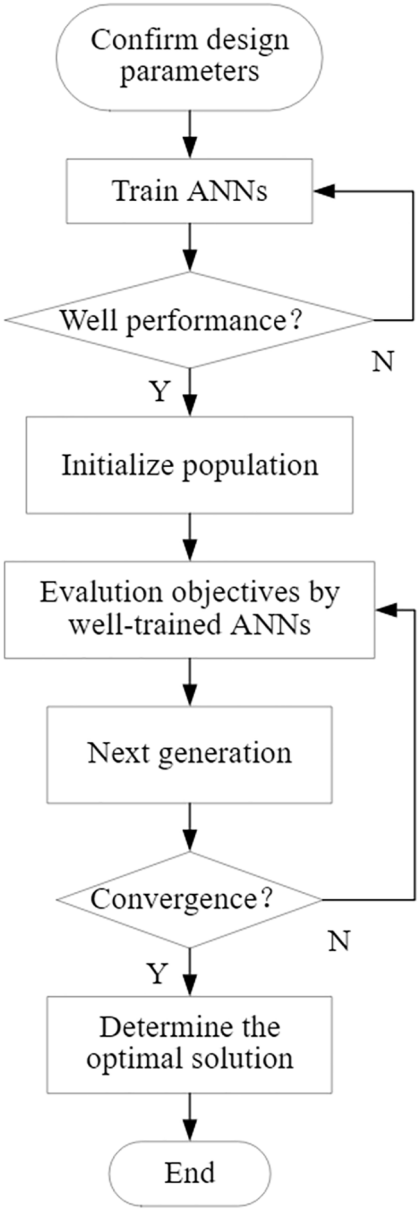

Fig. 5. Flow chart of geometrical parameters optimization.

3. Results and discussion

3.1. Heat transfer enhancement mechanism

The streamlines near the wall are shown in Fig. 6 (a). Obviously, guided by the micro fins, the helical flows are formed along with the helical direction in the gap area between two adjacent micro fins when the fluid flows from the front of the tube. This flow characteristic extends the fluid flow paths so that the fluid near the wall can be better heated by the wall. Moreover, as shown in Fig. 6 (b), the vortex structures are generated in the gap area because of the helical flows, which intensify the fluid disturbance and lead the boundary layers to be thinned and destroyed. On the other hand, the existence of a large number of starts dramatically increases the contact area between the fluid and heating surface. In a word, it can be considered that one of the sources of heat transfer enhancement in the HFT is secondary flow near the wall, and the other is the increasing area of the heat exchange surface.

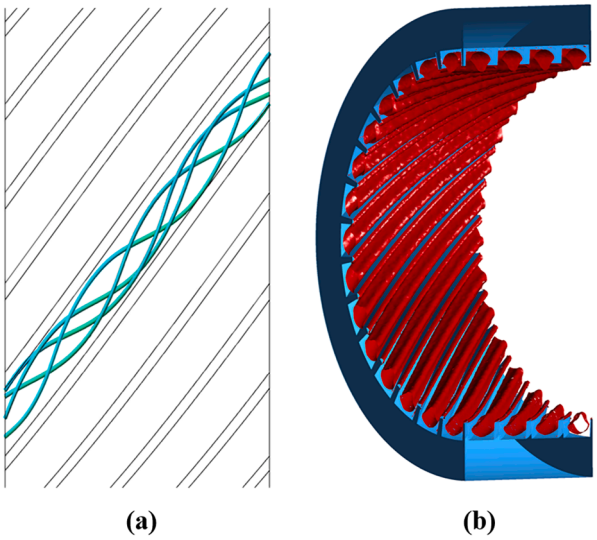

Fig. 6. Near-wall flow characteristics: (a) streamlines in the gap area between the micro fins; (b) isosurface vortex core region.

3.2. Effects of geometrical parameters

3.2.1. Effects of the micro fin height

To investigate the effects of micro fin height on the heat transfer and flow characteristics in the HFT, Fig. 7 shows the variations of the Nusselt number ratios, friction factor ratios, and *PEC* values with the different micro fin heights. On the whole, the variation trends of the Nusselt number ratios and friction factor ratios are exactly the same, which both show an increasing trend with the increase of the micro fin height. It suggests that the higher micro fins can improve the heat transfer performance, but it will cause great flow resistance at the same time. In addition, it can be clearly seen in Fig. 7 (a) that when the number of starts is small such as 30 or 40, the Nusselt number is more sensitive to the variation of the micro fin height. However, when the number of starts is pretty large, the effects of the micro fin height are visible only in the flow resistance, while having little attribution to the heat transfer enhancement. To analyze the reasons for these two different variations, Fig. 8 displays the turbulent kinetic energy and temperature distributions on the end surface of the HFT with the different micro fin heights at $Ns = 30$ and $\varphi = 20°$. Fig. 8 (a) illustrates that with the increase of the micro fin height, the turbulent kinetic energy in the top area of the micro fins increases significantly. This demonstrates that the disturbance in this region increases drastically, resulting in a stronger secondary flow. On the one hand, the stronger secondary flow will consume more mainstream speed, implying an increase in flow power consumption. On the other hand, the mixing of the hot fluid near the wall and the cold fluid in the mainstream domain will be aggravated owing to the secondary flow, giving rise to a better heat transfer performance. Combined with the discussion on the heat transfer enhanced mechanism, it can be observed that the increase of the micro fin height improves not merely the intensity of the secondary flow as well as the heat transfer area. When the HFT has fewer micro fins, these two factors account for the comparable proportions in the heat transfer enhancement mechanism. As a result, the increase of the micro fin height will simultaneously improve the heat transfer performance and flow resistance. When the HFT has a large number of starts, the heat exchange area is several times greater than that of the smooth tube. The increase in the heat transfer area will dominate the heat transfer enhancement mechanism. Besides, the increase in heat transfer area caused by the rise of the micro fin height is considerably smaller than that of the numerous micro fins, quantitatively. Hence, in this situation, the heat transfer capacity will not be drastically enhanced in spite of the increased height of the micro

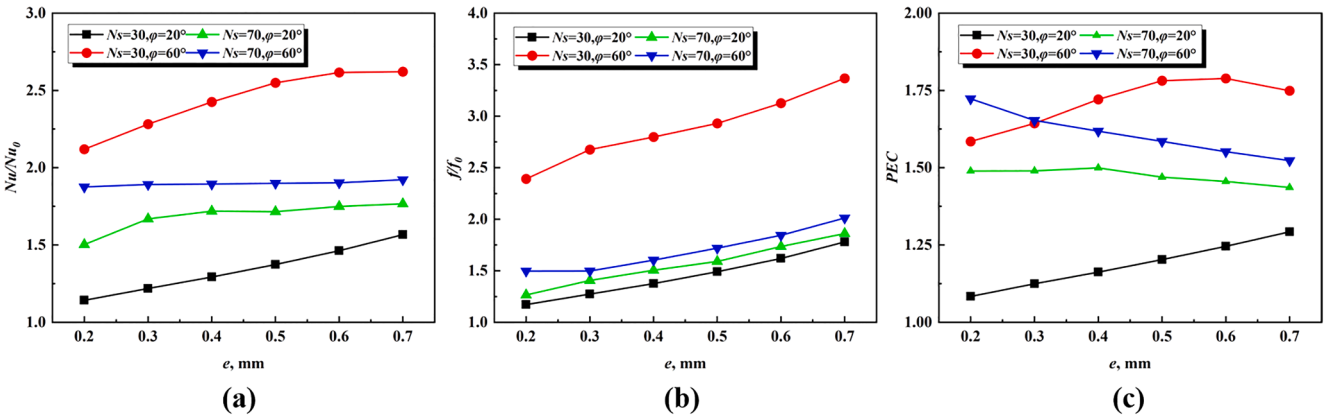

Fig. 7. Effects of the micro fin height: (a) Nusselt number ratio; (b) friction factor ratio; (c) PEC.

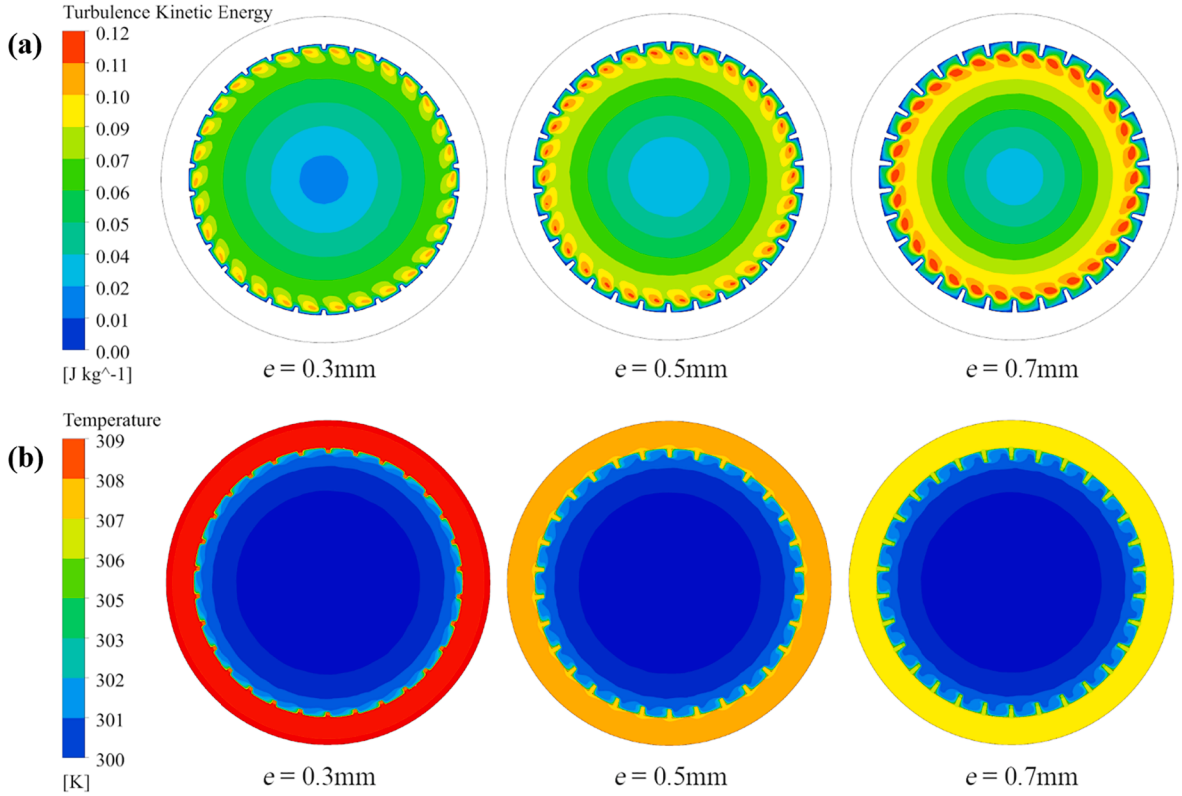

Fig. 8. Variables distributions with the different micro fin heights: (a) turbulent kinetic energy; (b) temperature.

fin.

The variation of the overall performance (*PEC*) with the micro fin height is shown in Fig. 7 (c). As depicted, the *PEC* value is greater than 1 in the given parameters range. It suggests that the HFT is a heat transfer enhanced tube with excellent overall performance. Furthermore, it is worth noting that the overall performance slightly increases with the increase of the micro fin height when the number of starts is lower. However, the variation trend is opposite to the previous case when the number of starts is far greater. Therefore, for a HFT with a small number of starts, in general, the overall performance can be improved by increasing the micro fin height. However, it should also be noted that when the helical angle is around 50–60°, the maximum value of the overall performance will reach the maximum value around 0.6 mm. In the case of a HFT with a large number of starts, a lower micro fin height should be adopted.

3.2.2. *Effects of the helical angle and the number of starts*

Fig. 9 illustrates the velocity and temperature distributions on the cross-section under the different micro fin pitches (*P*). As depicted in Fig. 9 (a), when the adjacent micro fins are far away from each other, the velocity of the fluid near the wall is quite high when the fluid flows through the groove area between the micro fins. The micro fins will produce disturbances only in the part base corners area, resulting in the most fluid domain in the inter-costal grooves being not affected. Meanwhile, the velocity vector in this area is substantially parallel to the wall. In other words, the intensity of the secondary flow near the wall is relatively small, and the heat transfer performance of the entire tube will not be significantly improved. Additionally, when the distance between two adjacent micro fins is extremely small, the velocity of the fluid in the groove area is close to zero. This indicates that part of the fluid is constrained in the groove area and is difficult to be carried away by the mainstream fluid. The geometrical structure of helical micro fins is filled

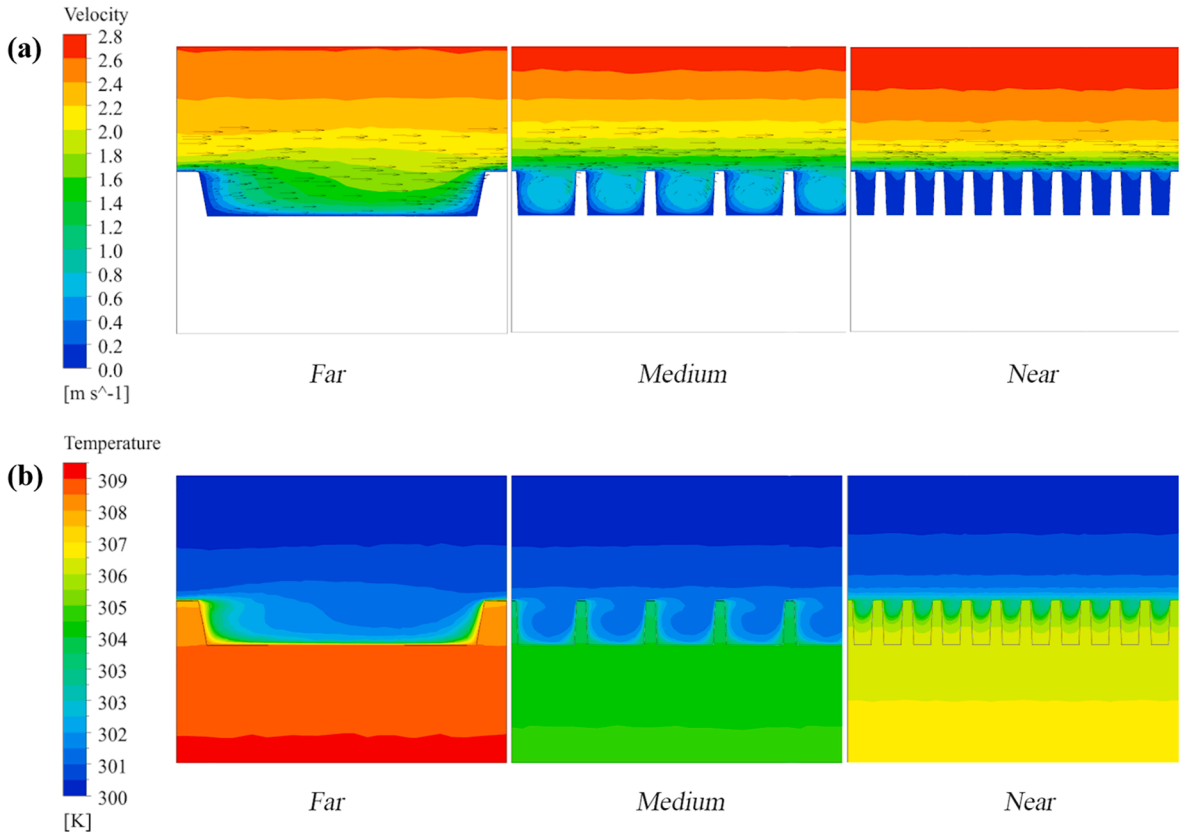

Fig. 9. Variables distributions with the different micro fin pitches: (a) velocity magnitude and velocity vector; (b) temperature.

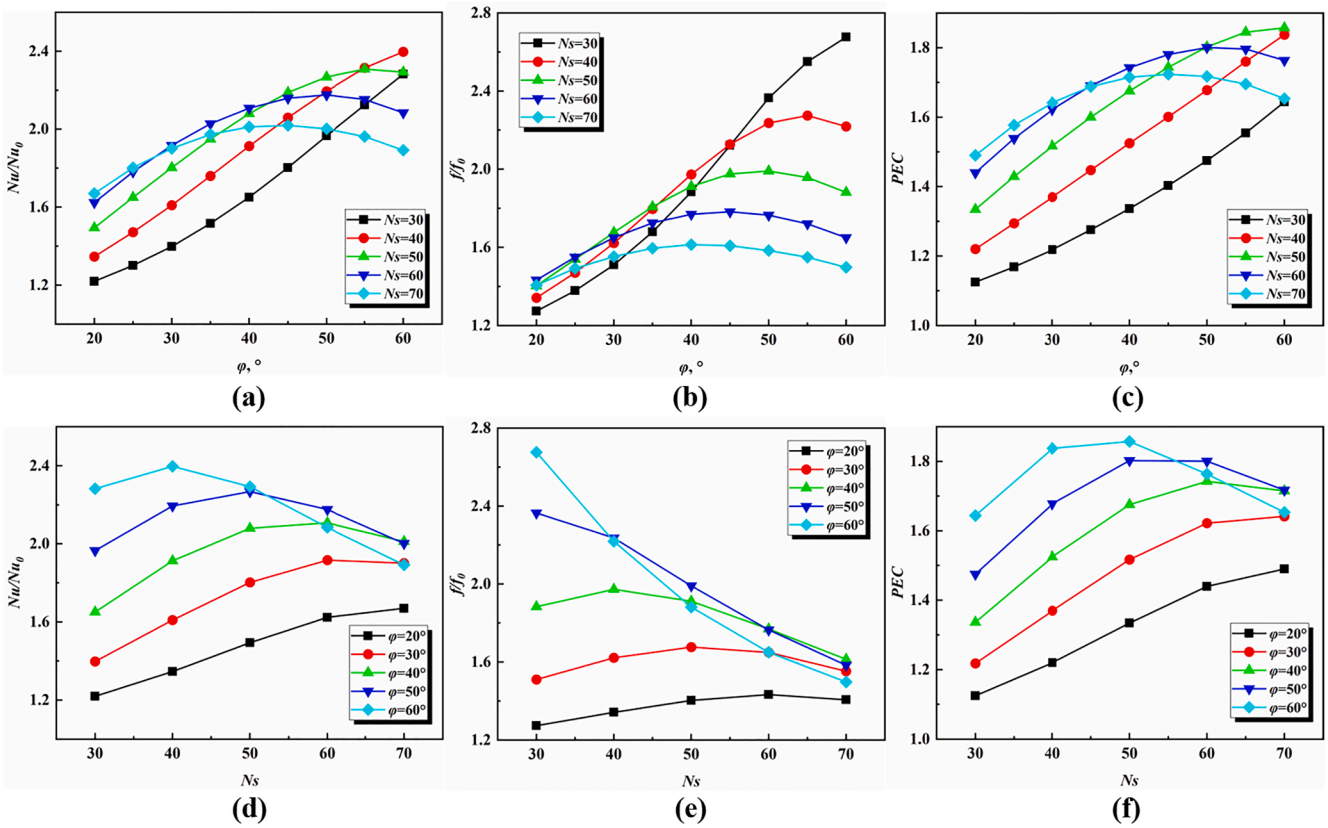

Fig. 10. Effects of the helical angle: (a) Nusselt number ratio; (b) friction factor ratio; (c) PEC; and effects of the number of starts: (d) Nusselt number ratio; (e) friction factor ratio; (f) PEC.

with this part of the fluid, which is similar to the smooth tube. Only when the distance is within a proper range, an intense secondary flow will be generated near the wall, which significantly enhances the heat transfer. It can be clearly seen in Fig. 9 (b) that the average temperature of the model with the medium distance is evidently lower than the model with small or large ones. The distance (P) is given by Eq. (1). Obviously, the two geometrical parameters (Ns and φ) should be considered together.

Fig. 10 displays the heat transfer and flow performance with the different helical angles and numbers of starts at $e = 0.3$ mm. As illustrated in Fig. 10 (a) and Fig. 10 (b), when the number of starts is small, such as 30 or 40, the P value is in a larger range (P greater than 0.7 mm) according to Eq. (1). The increase of the helical angle will reduce the P value. As a result, the intensity of the secondary flow will increase, which will improve the heat transfer capacity and flow resistance. Besides, the variation of the helical angle does not affect the heat exchange area. So the final result is that the Nusselt number, friction factor, and overall performance are all increased. On the other hand, the P value is already close to the optimal value ($P_{opt} = 0.7$ mm) when the number of starts is relatively large, such as 60 or 70. In this case, with the increase of the helical angle, the P value will decrease from the initial larger range until the vlaue passes through the optimal range, and enters the smaller range. Hence, the intensity of the secondary flow will increase first and then decrease. However, the heat exchange area remains unchanged. The final result is that the Nusselt number, friction factor, and overall performance all show a trend of increasing first and then decreasing, with reaching their maximum values at the helical angle of 40 to 50°. Therefore, we can conclude that a larger helical angle should be adopted when the number of starts is small (Ns is around 30–50), and the helical angle should be set to 40–50°when the HFT involves many micro fins (Ns is greater than 50).

Similar to the helical angle, the effects of the number of starts should be discussed on a case by case basis. As depicted in Fig. 10 (d) and (e), when the helical angle is small, such as 20 or 30°, the P value is in a relatively larger range (P greater than 0.7 mm). As the number of starts increases, the P value will decrease, but the intensity of the secondary flow will increase. Different from the helical angle, the increase of the number of starts will significantly increase the heat exchange area. These two factors lead the Nusselt number, friction factor, and overall performance to increase together. When the helical angle is large, such as 50 or 60°, the P value is in an extremely small range ($P < 0.7$ mm). As the number of starts increases, the P value becomes further small. Consequently, the intensity of secondary flow near the wall decreases, and the flow resistance will decrease as well. However, the heat exchange area is increasing all the time. That is to say, in the heat transfer enhancement mechanism, the increased heat transfer area will have a positive effect, while the secondary flow exhibits a suppressive effect. The final result is that the heat transfer performance will increase first and then decrease, but the flow resistance will always decrease. A conclusion can also be drawn here. When the helical angle is small, the heat transfer performance can be enhanced by increasing the number of starts. Combined with the previous conclusions, the optimal geometrical parameters range of the HFT can be summarized, that is, the helical angle and the number of starts will be around 40°and 60, respectively, and a lower micro fin height should be adopted.

3.3. Exergy destruction analyses

Fig. 11 presents the local exergy destruction rate distributions of the smooth tube and HFT caused by heat transfer (the thermal dissipation

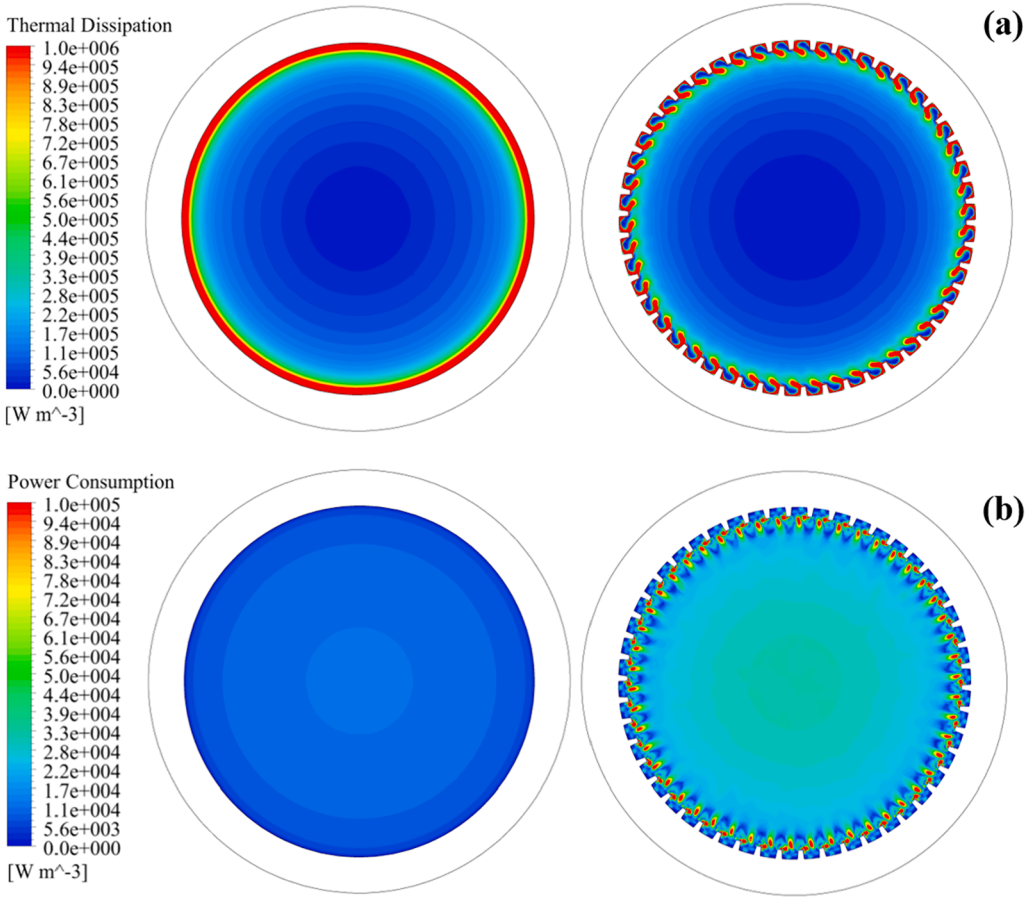

Fig. 11. Local exergy destruction rate distributions: (a) local thermal dissipation; (b) local power consumption.

$E_{xd,\Delta T}$) and fluid flow (the power consumption $E_{xd,\Delta p}$). The local thermal dissipation has a great dependence with the corresponding temperature contour. A higher local thermal dissipation will be expected in the region with the high temperature gradient. The local power consumption is related to the synergy between the velocity vector and pressure gradient of the fluid clusters. The stronger the disturbance is, the higher the local power consumption will be. On account of the proximity to the heating wall, the temperature gradient in the top area of the micro fins is large, and the local thermal dissipation demonstrates a higher value as well. On the other hand, the secondary flow is generated because of the micro fins, increasing the disturbance in this area. Thus, the local power consumption near will be increased. Besides, owing to the secondary flow, the interaction between the fluid clusters is enhanced, so the average thermal dissipation and average power consumption of the HFT will be lower and higher than that of the smooth tube, respectively.

Fig. 12 illustrates the relationship between the equivalent heat transfer coefficient and average thermal dissipation and the relationship between the unit pressure drop and average power consumption during the different micro fin heights and helical angles at $Ns = 30$. Obviously, the equivalent heat transfer coefficient and average thermal dissipation roughly show a negative correlation. The greater the equivalent heat transfer coefficient is, the smaller the temperature difference between the fluid and the heating wall is, and the smaller the average thermal dissipation will be. Therefore, the variation of the average thermal dissipation with the geometrical parameters is exactly opposite of the equivalent heat transfer coefficient. From the physical view, the unit pressure drop reflects the power consumption of the entire tube. Thus, as shown in Fig. 12 (b), the unit pressure drop and average power consumption exhibit a strict positive correlation and the variation of average power consumption is almost consistent with the unit pressure drop. In brief, the effects of geometrical parameters on exergy destruction can be obtained by the previous parametric analysis, so it won't be repeated here.

3.4. Results of geometrical parameters optimization

3.4.1. Analysis of ANNs

As shown in Table 2, considering the wide range of the optimal helical angle obtained by the previous parametric analysis, in the feasible region of the parameters, 6, 9, and 5 levels are selected for the micro fin height, the helical angle, and the number of starts, respectively. A total of 270 complete numerical experiments are carried out by coupling Python and Fluent so as to set up and execute the simulations automatically. And the 270 sets of numerical data are used as the sample data of the ANNs.

Table 2
Selected values of design variables for numerical simulations.

Variables	Values
e, mm	0.2, 0.3, 0.4, 0.5, 0.6, 0.7
φ, °	20, 25, 30, 35, 40, 45, 50, 55, 60
Ns	30, 40, 50, 60, 70

In the process of fitting, the number of neurons in the hidden layer has a great impact on the performance of the entire ANN. Too few neurons are prone to the under-fitting, which make the ANN cannot fully catch the data characteristics. Too many neurons make the ANN appear to the over-fitting. Both of them will lead to a deterioration in the overall performance of the ANN. To make full use of the sample data and avoid the under-fitting and over-fitting, this section conducts a comparative test on the number of neurons in the hidden layer. After dividing the sample data into five groups, one group is selected in turn as the testing set, and the rest groups are used as the training set. The average evaluation indicators of these ANNs are considered as the final performance of the number of neurons in the hidden layer. As shown in Fig. 13, with the increase of the network scales, the accuracy of the training set of the two optimization objectives gradually increases, and the accuracy of the testing set roughly increases first and then decreases. That is to say, during too small and too large network scales, the under-fitting and over-fitting probably occur in the ANNs. According to the accuracy of the testing set, the proper scales are determined, that is, the ANN of J_1 (or J_2) contains 19 (or 16) neurons in the hidden layer. Besides, the parameters (weights and biases) of the selected ANNs have been given in Table 3.

To further ensure that the obtained ANNs have the higher prediction accuracy, the prediction values of the ANNs are compared with the results obtained by the numerical simulations. The comparison results are shown in Fig. 14. It can be seen that the data predicted by the ANNs and the results obtained by the numerical simulation are in excellent agreement. The maximum deviations of J_1 and J_2 are 3.26% and 5.49%, respectively. Meanwhile, the MSE and R^2 are very close to 0 and 1, respectively. As a result, the ANNs can meet the demands of subsequent optimization research.

3.4.2. Analysis of multi-objective optimization results

The multi-objective optimization problem can be described as:

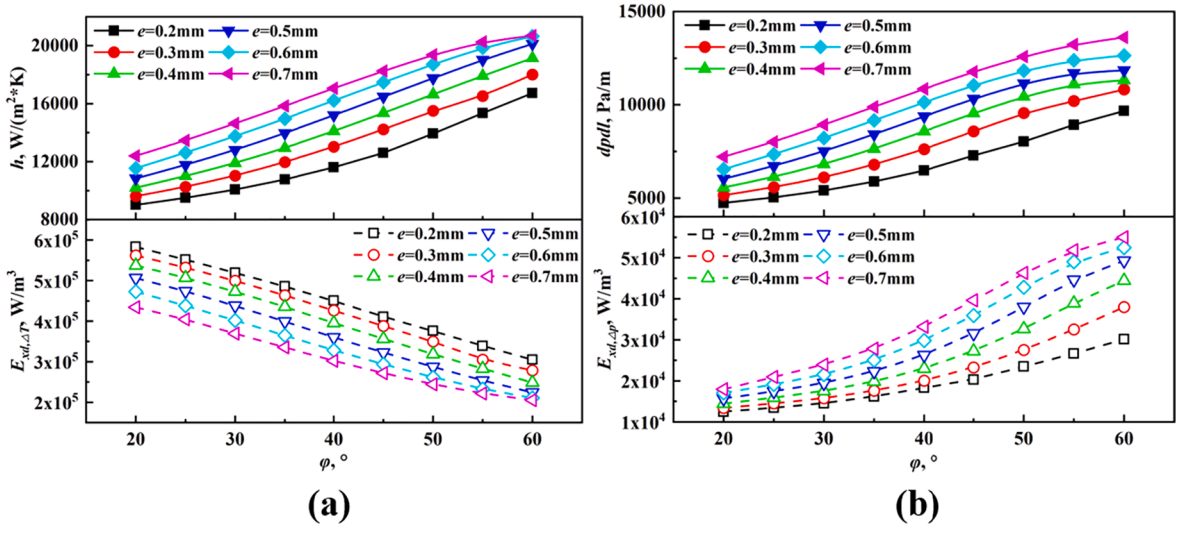

Fig. 12. Relationship between the thermal–hydraulic performance and exergy destruction: (a) average thermal dissipation and equivalent heat transfer coefficient; (b) average power consumption and unit pressure drop.

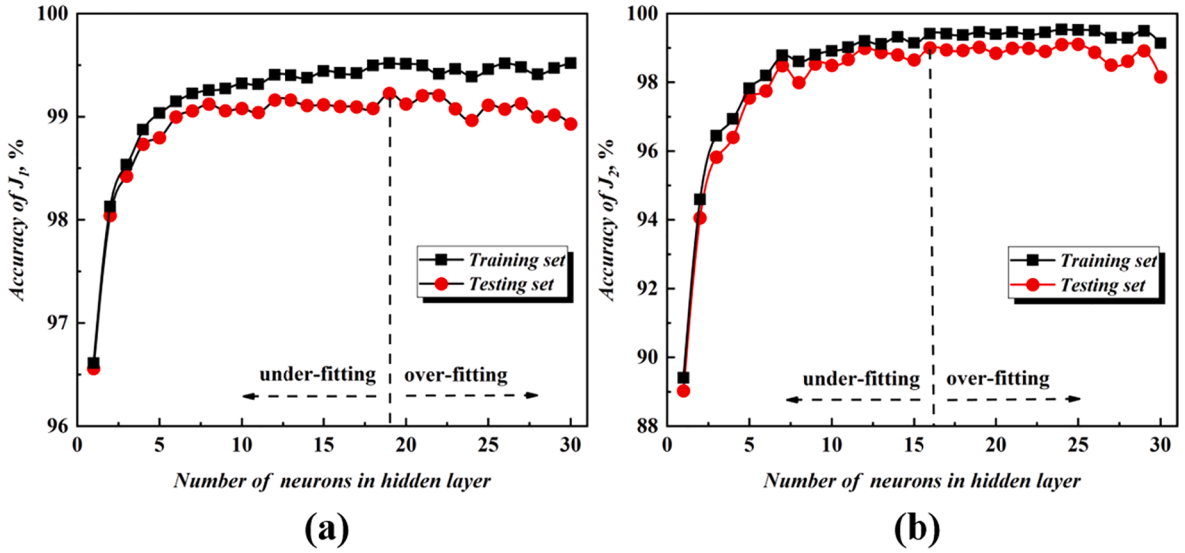

Fig. 13. Results of the different network scales: (a) J_1; (b) J_2.

Table 3
Parameters of the ANNs for the prediction of J_1 and J_2.

j	J_1					J_2				
	w_{ji}			b_k	0.5359	w_{ji}			b_k	−0.0333
	e	φ	Ns	b_j	w_{1j}	e	φ	Ns	b_j	w_{1j}
1	−4.6305	1.1692	2.2188	−6.6075	0.2141	−1.1886	2.4213	−1.3051	3.6960	0.1188
2	1.3239	1.6720	2.4047	−1.9876	−1.1113	−2.6511	0.1871	−1.5503	2.5795	−0.0847
3	0.8306	1.6414	2.2596	−1.8690	1.0526	−0.2281	−2.0743	−0.8793	1.7785	0.3000
4	−2.0834	1.3966	−0.7324	1.8669	−0.1322	−2.6780	1.1951	1.0698	−2.3449	−0.0374
5	−1.5382	−0.7618	−1.2525	0.4663	−0.8117	0.3401	1.3483	−0.0209	−0.5411	0.3310
6	1.6363	3.8736	2.9307	−2.5308	0.0461	−0.5613	1.7825	−1.4189	1.0223	0.0936
7	0.0744	2.2539	0.5658	−0.6545	−0.1578	0.7659	−0.3241	−2.0914	0.1760	0.0542
8	−1.2185	−2.2768	0.1677	−2.6433	0.0986	−0.7545	−2.2215	−2.5110	−1.3376	−0.0447
9	−0.0145	−1.5500	−2.3285	0.0239	−0.1581	−3.1543	−0.1121	−0.7297	−0.0633	−0.0251
10	1.9427	1.4719	2.0583	−0.3492	−0.4628	2.9921	−1.7291	−0.6391	−0.8762	0.0102
11	−0.4277	−1.1949	−0.5441	−0.7044	0.4530	0.7293	−0.8672	1.1511	1.3536	−0.1209
12	−1.2259	−0.9509	−1.6974	−0.9071	0.4703	2.1750	2.8630	−0.7657	−2.3575	0.0345
13	−1.5556	−0.6099	1.0306	1.7485	−0.0557	−0.5276	−0.9955	1.0388	2.3813	−0.7393
14	−3.2048	−1.5256	2.3935	1.3073	0.0024	3.2202	−0.0012	0.8703	2.6895	0.0698
15	−2.0432	4.5108	−0.4950	−3.9677	0.0454	−0.6199	−0.9902	−3.5144	−2.8149	−0.1111
16	−0.9476	−0.3881	−3.3669	−2.9088	0.1322	2.6786	1.7661	2.0875	2.0687	0.0641
17	−3.1541	1.6603	−0.3640	2.6642	0.1029	–	–	–	–	–
18	−1.1158	1.3300	3.9876	2.7875	0.0294	–	–	–	–	–
19	−0.5861	3.5331	−0.5977	−3.5061	−0.1238	–	–	–	–	–

Minimization: $J_1 = f_1(e,\ \varphi,\ Ns)$ and $J_2 = f_2(e,\ \varphi,\ Ns)$

Subject to: $e \in [0.2,\ 0.6]$, $\varphi \in [20,\ 60]$ and $Ns \in [30,\ 70]$

where f_1 and f_2 represent the ANNs fitted to J_1 and J_2. obtained in the previous section, respectively.

Considering that the number of starts must be an integer in practical applications, so it should be rounded during the optimization process. In order to optimize the two opposing optimization objectives, the fast non-dominated sorting genetic algorithm with elite strategy (NSGA-II) is adopted. The specific process of the NSGA-II is referenced [39]. Some operating parameters of the algorithm are shown in Table 4.

Finally, the Pareto front solved by the NSGA-II is shown in Fig. 15, which contains 40 non-inferior solutions. It is noted that every point on the Pareto front is a global optimal solution in the parameters feasible region. When moving from an optimal solution to another one, the variations of the two optimization objectives are bound to be opposite. There is no difference in advantage between them, only the values of the corresponding optimization objectives will be different. This indicates that the best solution cannot be chosen from the Pareto front according to the fitness values because of the non-dominance. Furthermore, the further reduction in the optimization objectives is much more difficult at each end of the Pareto front, which means that a solution with the best compromise performance may exist between end points. Therefore, this section adopts a classic decision-making algorithm (TOPSIS) to obtain the optimal solution. The specific process of the TOPSIS is referenced [40,41]. The algorithm detects the distance between the ideal optimal solution and the ideal worst solution. If a rating scheme is closest to the optimal solution and far away from the worst solution, it is considered the optimal scheme. In the present work, the two optimization objectives are considered to have equal relative importance according to the literature [42]. Thus, the weighting matrix is [0.5 0.5]. The relative closeness values to the ideal optimal solution are shown in the blue points in Fig. 15, which vary from 0.354 to 0.782. Besides, it is found that the solutions at the end points of the Pareto front contain lower relative closeness, which means improving the particular performance merely will lead to a decline in the overall performance. Therefore, point B on the Pareto front is selected as the best compromise solution, which obtains the highest relative closeness value.

The distributions of design variables corresponding to the Pareto

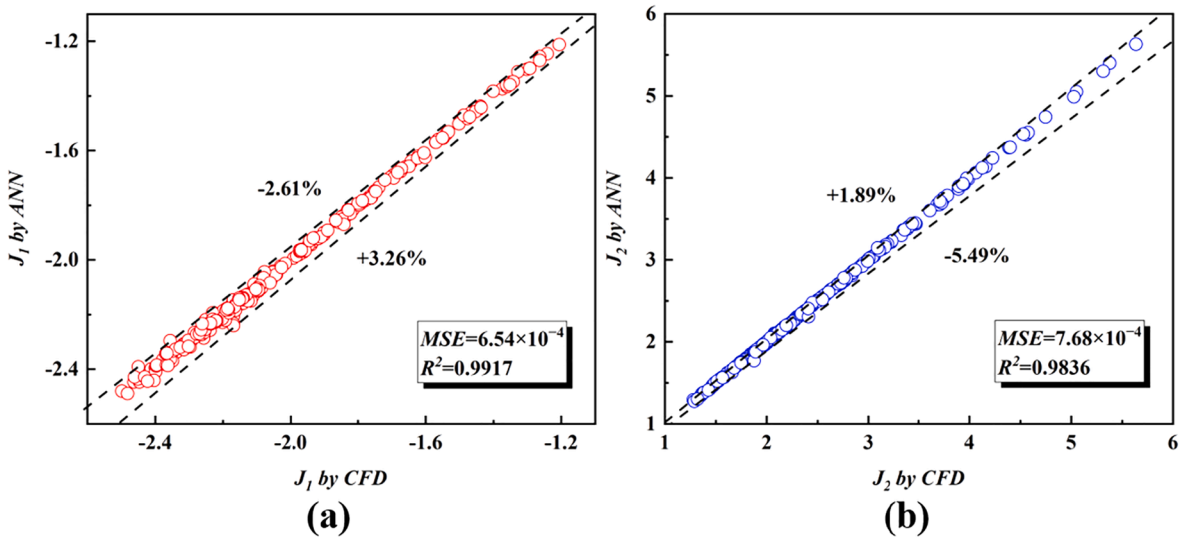

Fig. 14. Comparisons between numerical simulations and ANN prediction values: (a) J_1; (b) J_2.

Table 4
Parameter settings of NSGA-II.

Parameters	Values
Population Size	200
Pareto Factor	0.2
Crossover Fraction	0.8
Migration Fraction	0.2
Generations	1000
Function Tolerance	10^{-4}

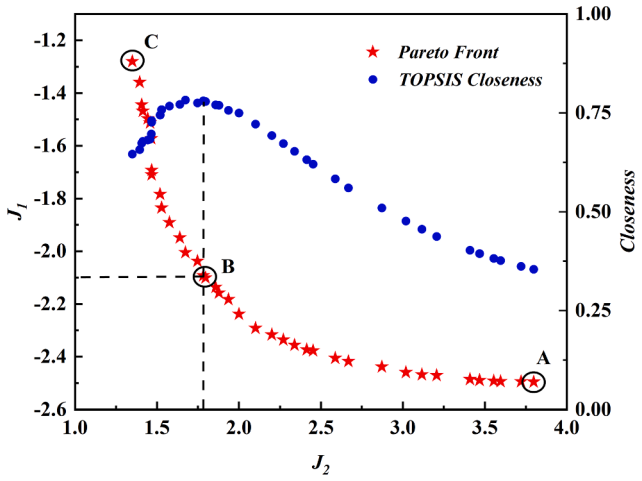

Fig. 15. Pareto front obtained by NSGA-II.

Front solutions are illustrated in Fig. 16. As shown in Fig. 16 (b), the number of starts and helical angle roughly show a U-shaped distribution, that is, the optimal values of the number of starts and the helical angle will remain constant in some range classes, they are corresponding to $Ns = 65$ and $\varphi = 20°$ or $60°$, respectively. It suggests that the overall performance of the helical micro fin tubes may be much higher when the geometric parameters are taken close to these values. As a whole, the relationship between the number of starts and the helical angle on the Pareto Front is rather chaotic. It may be related to the fact that the variation of the number of starts have an impact on the disturbance and heat transfer area near the inner wall, while the variation of the helical angle will only affect the disturbance. At the same time, they have different variation trends on heat transfer and flow characteristics and the proportion may be different as well. On the other hand, as can be seen from Fig. 16 (d), the number of starts and micro fin height approximately exhibit a V-shaped distribution. Hence, the tube type with a larger number of starts and a lower micro height, as well as the type with a smaller number of starts and a higher rib height, may be the ones with excellent overall performance. To sum up, the geometrical parameters of helical micro fin tubes are strongly coupled to each other. It is pretty difficult to analyze them individually, which confirms the conclusion of the previous parametric analysis.

To evaluate the overall performance of the optimal solution selected by TOPSIS, we compare the optimization objectives values of three different solutions: the J_1 minimization, the J_2 minimization, and the optimal TOPSIS solutions. The geometrical parameters of these solutions are listed in Table 5, and the results are shown in Fig. 17. Obviously, compared with the J_1 minimization solution, J_2 of the TOPSIS solution can be reduced by 53.1% with an increase of 16.2% in J_1. Compared with the J_2 minimization solution, even though J_2 increases by 32.0%, J_1 can be further reduced by 63.5%. Hence, the TOPSIS solution is the best compromise one for lowering the thermal dissipation of the Pareto Front solutions without increasing power consumption significantly.

3.4.3. Comparison with previous optimization studies

To objectively evaluate the thermal–hydraulic performance of the optimal result obtained in this work, Table 6 lists the results of several researchers for the geometrical parameters optimization of the HFT. Taking into account the differences in different kinds of literature, such as fluid working conditions, inner and outer diameters of the tubes, and geometrical parameters optimization ranges, the optimal results are further processed to compare their performance. The No. 1 tube is calculated according to the equations, which are the relation formula of the optimal geometrical parameters proposed by Dastmalchi et al. [14]. The No. 2 and No. 3 tubes are given by selecting higher *PEC* values from the Pareto front obtained by Garrett et al. [15]. In particular, as for the No. 4 tube, in the work of Jasiński et al. [26], only the helical angle was optimized, the micro fin height and the number of starts were directly determined by empirical values. It can be noted that compared with the previous researches, the optimal type in this work tends to have a larger number of starts and a lower micro fin height. This type of HFT has been proved to be a better choice in the parametrical analysis in Section 3.2. To intuitively compare the performance of these HFTs, we use these geometrical parameters listed in Table 6 to carry out numerical simulations again. Due to the large difference between the inner diameter of

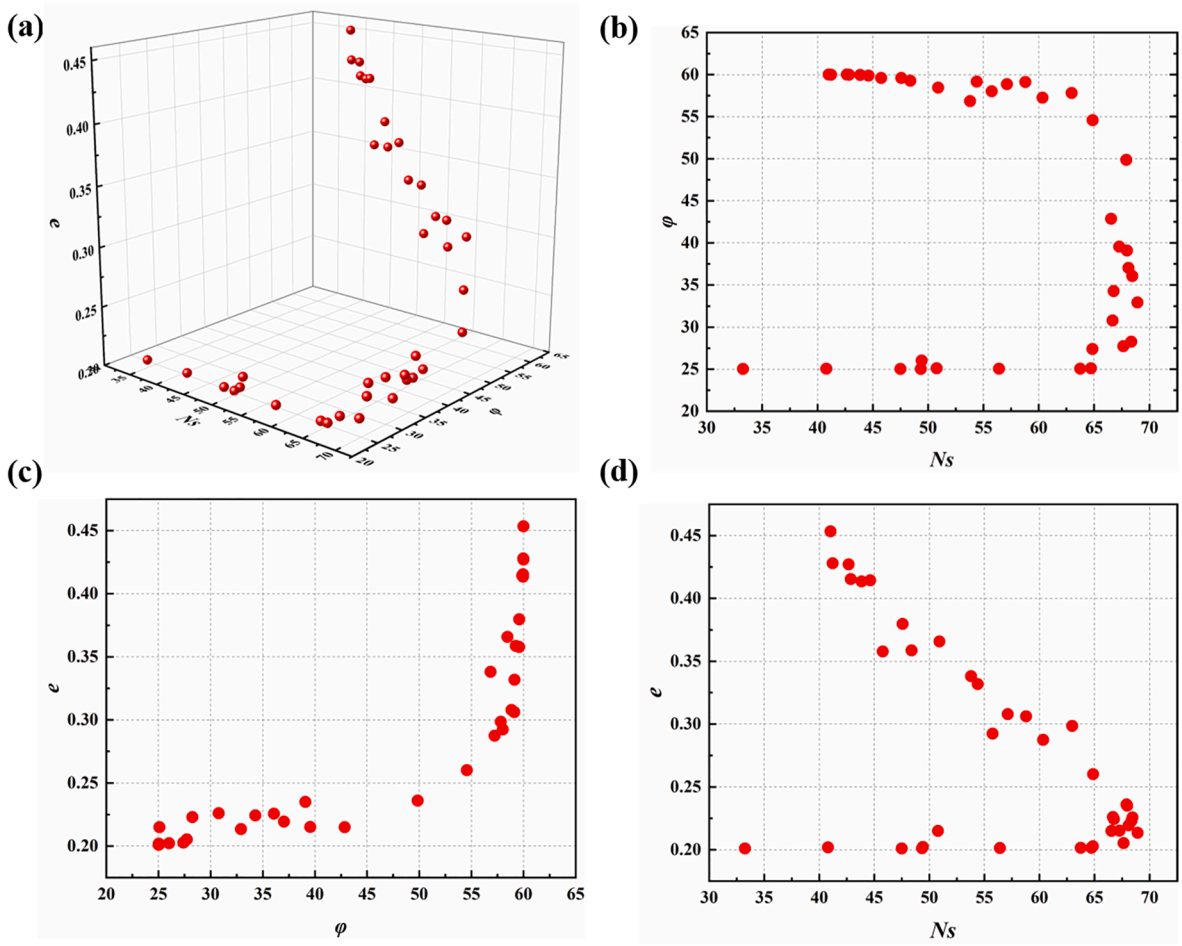

Fig. 16. Distributions of design variables corresponding to the Pareto Front solutions: (a) *Ns* - *φ* - *e*; (b) *Ns* - *φ*; (b) *φ* - *e*; (d) *Ns* - *e*.

Table 5
Geometrical parameters of the different solutions.

Solutions	Geometrical parameters		
	e	*φ*	*Ns*
A(J_1 minimization)	0.45	59.9	41
B(TOPSIS)	0.23	36.1	66
C(J_2 minimization)	0.20	25.0	33

the No. 4 tube and the other tubes, the micro fin height of the No. 4 tube is converted according to the same $\frac{e}{D_i}$ value during the modeling process, while the helical angle and number of starts remain unchanged. As shown in Fig. 18, the Nusselt number of the optimal tube type obtained in this work is higher than that of the No. 1 tube but lower than that of the other tubes. However, the friction factor is relatively small, especially when the Reynolds number is around 20,000–36,000. In a word, the optimal tube obtained in this work provides a relatively effective heat transfer enhancement without a significant increase in flow resistance.

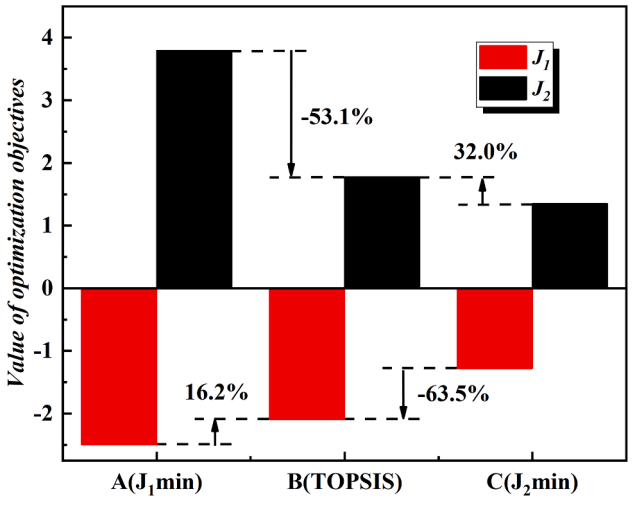

Fig. 17. Performances of the different solutions.

4. Conclusions

In this work, numerical simulations are carried out to investigate the effects of the geometrical parameters on the thermal–hydraulic performance and the exergy destruction. As a result, the gap of heat transfer and the geometrical optimization study of HFT based on the second law of thermodynamics is filled. Besides, this work provides strong evidence that the exergy destruction minimization principle is still applicable in the case of the periodic model and fully developed turbulence, which was lacking in previous literature. The main conclusions are as follows:

(1) The variation ranges of Nu/Nu_0, f/f_0, and overall performance for the helical micro fin tube (HFT) are 1.14–2.62, 1.17–3.37, 1.08–1.87 at $Re = 36{,}636$, respectively. It means the HFT is a kind of enhanced tube with excellent overall performance.

Table 6
Optimal results of the different researchers.

No	Authors	Optimization objective(s)	Working conditions		Optimal results			Ref
			Re	D_i	*e*	φ	*Ns*	
#1	Dastmalchi et al.(2017)	$\frac{h/h_0}{f/f_0}$	36,636	15.6	0.50	18.8	60	[14]
#2	Garrett et al.(2019)	$\frac{Nu}{Nu_0},\frac{f}{f_0}$	49,013	15.54	0.29	35.6	63	[15]
#3			49,013	15.54	0.29	51.2	61	
#4	Jasiński et al.(2011)	$\frac{S_{gen}}{S_{gen,0}}$	–	11.5	0.25	70	65	[26]
#5	Present work	$-\frac{E_{xd,\Delta T,0}}{E_{xd,\Delta T}},\frac{E_{xd,\Delta p}}{E_{xd,\Delta p,0}}$	36,636	15.6	0.23	36.1	66	–

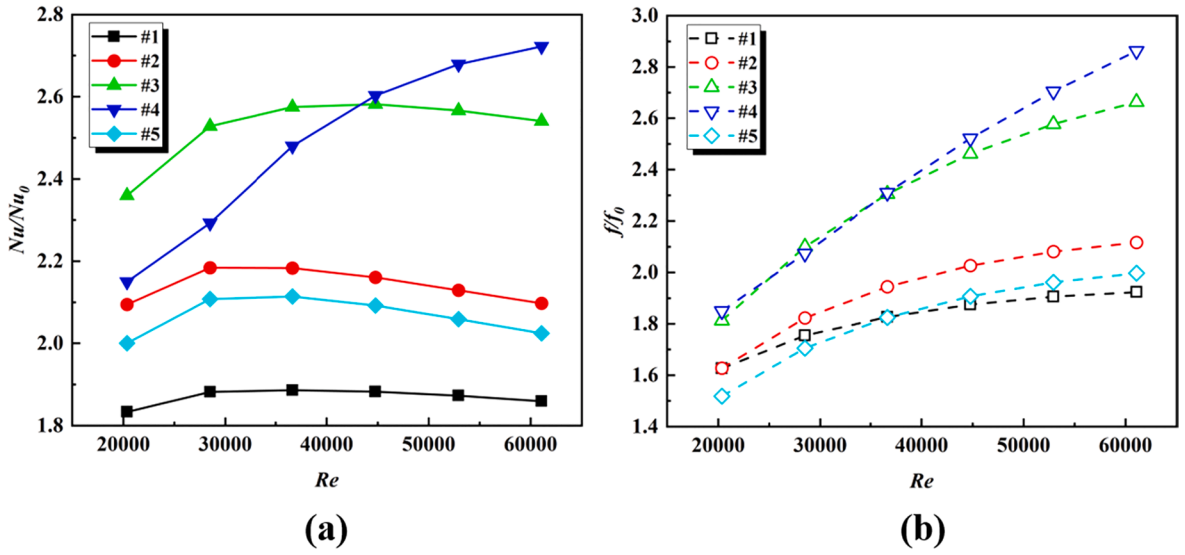

Fig. 18. Results of the different researchers: (a) Nusselt number ratio; (b) friction factor ratio.

(2) According to the parametric analysis, with the increase of the micro fin height (*e*), the heat transfer performance and flow resistance increase as well, and they will be more sensitive at a lower number of starts. Moreover, the number of starts (*Ns*) and helical angle (φ) should be considered together because of the strong mutual coupling between them.
(3) The local exergy destruction rates of the HFT caused by heat transfer (the thermal dissipation $E_{xd,\Delta T}$) and fluid flow (the power consumption $E_{xd,\Delta p}$) are mainly concentrated in the top area of micro fins near the wall. In addition, the average thermal dissipation roughly shows a negative correlation with the equivalent heat transfer coefficient, while the average power consumption shows a strict positive correlation with the unit pressure drop.
(4) The Pareto front for the average thermal dissipation reduction rate and the average power consumption increase rate is obtained. The geometrical parameters ($e = 0.23$ mm, $\varphi = 36.1°$, and $Ns = 66$) are chosen as the optimal solution by using the TOPSIS method, whose *PEC* value can reach 1.73. Furthermore, compared with the optimal tube types in the published literature, the optimal type in this work tends to have a larger number of starts and a lower micro fin height.

CRediT authorship contribution statement

J.H. Xie: Methodology, Software, Validation, Formal analysis, Investigation, Data curation, Writing – original draft, Writing – review & editing. **H.C. Cui:** Methodology, Software, Data curation. **Z.C. Liu:** Supervision, Project administration, Funding acquisition. **W. Liu:** Conceptualization, Resources, Supervision, Project administration, Funding acquisition.

Declaration of Competing Interest

The authors declare that they have no known competing financial interests or personal relationships that could have appeared to influence the work reported in this paper.

Acknowledgement

This work is supported by the National Natural Science Foundation of China (grant no. 51736004).

References

[1] J.I. Córcoles-Tendero, J.F. Belmonte, A.E. Molina, J.A. Almendros-Ibáñez, Numerical simulation of the heat transfer process in a corrugated tube, Int J Therm Sci 126 (2018) 125–136.
[2] K. Navickaitė, L. Cattani, C.R.H. Bahl, K. Engelbrecht, Elliptical double corrugated tubes for enhanced heat transfer, Int J Heat Mass Tran 128 (2019) 363–377.
[3] X. Shuai, L. Zheng, Z. Liang, Y. Wang, D. Hu, Z. Jie, Numerical investigation on heat transfer performance and flow characteristics in enhanced tube with dimples and protrusions, Int J Heat Mass Tran 122 (2018) 602–613.
[4] K. Aroonrat, C. Jumpholkul, R. Leelaprachakul, A.S. Dalkilic, O. Mahian, S. Wongwises, Heat transfer and single-phase flow in internally grooved tubes, Int Commun Heat Mass 42 (2013) 62–68.
[5] S. Pethkool, S. Eiamsa-ard, S. Kwankaomeng, P. Promvonge, Turbulent heat transfer enhancement in a heat exchanger using helically corrugated tube, Int Commun Heat Mass 38 (2011) 340–347.
[6] A.T. Wijayanta, I. Yaningsih, M. Aziz, T. Miyazaki, S. Koyama, Double-sided delta-wing tape inserts to enhance convective heat transfer and fluid flow characteristics of a double-pipe heat exchanger, Appl. Therm. Eng. 145 (2018) 27–37.
[7] S. Eiamsa-ard, W. Changcharoen, R. Beigzadeh, P. Eiamsa-ard, K. Wongcharee, V. Chuwattanakul, Influence of co/counter arrangements of multiple twisted-tape

bundles on heat transfer intensification, Chemical Engineering and Processing - Process Intensification 160 (2021), 108304.
[8] W.T. Ji, A.M. Jacobi, Y.L. He, W.Q. Tao, Summary and evaluation on single-phase heat transfer enhancement techniques of liquid laminar and turbulent pipe flow, Int J Heat Mass Tran 88 (2015) 735–754.
[9] R.L. Webb, R. Narayanamurthy, P. Thors, Heat transfer and friction characteristics of internal helical-rib roughness, Journal of Heat Transfer-Transactions of the Asme 122 (2000) 134–142.
[10] G.J. Zdaniuk, L.M. Chamra, P.J. Mago, Experimental determination of heat transfer and friction in helically-finned tubes, Exp. Therm Fluid Sci. 32 (2008) 761–775.
[11] W.T. Ji, D.C. Zhang, Y.L. He, W.Q. Tao, Prediction of fully developed turbulent heat transfer of internal helically ribbed tubes - An extension of Gnielinski equation, Int J Heat Mass Tran 55 (2012) 1375–1384.
[12] Z. Hernadi, G. Kristof, Prediction of pressure drop and heat transfer coefficient in helically grooved heat exchanger tubes using large eddy simulation, Proc. Inst. Mech. Eng. Part A-J. Power Energy 228 (2014) 317–327.
[13] W. Li, P. Fu, H. Li, G. Li, P. Thors, Numerical-Theoretical Analysis of Heat Transfer, Pressure Drop, and Fouling in Internal Helically Ribbed Tubes of Different Geometries, Heat Transfer Eng 37 (2016) 279–289.
[14] M. Dastmalchi, G.A. Sheikhzadeh, A. Arefmanesh, Optimization of micro-finned tubes in double pipe heat exchangers using particle swarm algorithm, Appl. Therm. Eng. 119 (2017) 1–9.
[15] G.W. Mann, S. Eckels, Multi-objective heat transfer optimization of 2D helical micro-fins using NSGA-II, Int. J. Heat Mass Transf. 132 (2019) 1250–1261.
[16] H. Safikhani, S. Eiamsa-ard, Pareto based multi-objective optimization of turbulent heat transfer flow in helically corrugated tubes, Appl. Therm. Eng. 95 (2016) 275–280.
[17] H. Zarea, F.M. Kashkooli, M. Soltani, M. Rezaeian, A novel single and multi-objective optimization approach based on Bees Algorithm Hybrid with Particle Swarm Optimization (BAHPSO): Application to thermal-economic design of plate fin heat exchangers, Int J Therm Sci 129 (2018) 552–564.
[18] P. Ocłoń, S. Łopata, T. Stelmach, M. Li, J.-F. Zhang, H. Mzad, W.-Q. Tao, Design optimization of a high-temperature fin-and-tube heat exchanger manifold – A case study, Energy 215 (2021), 119059.
[19] B.S. Mekki, J. Langer, S. Lynch, Genetic algorithm based topology optimization of heat exchanger fins used in aerospace applications, Int J Heat Mass Tran 170 (2021), 121002.
[20] A. Bejan, Entropy generation minimization: The new thermodynamics of finite-size devices and finite-time processes, J. Appl. Phys. 79 (1996) 1191–1218.
[21] S. Zhou, L. Chen, F. Sun, Constructal entropy generation minimization for heat and mass transfer in a solid–gas reactor based on triangular element, J. Phys. D Appl. Phys. 40 (2007) 3545–3550.
[22] Z.Y. Guo, H.Y. Zhu, X.G. Liang, Entransy—A physical quantity describing heat transfer ability, Int J Heat Mass Tran 50 (2007) 2545–2556.
[23] W. Liu, P. Liu, J.B. Wang, N.B. Zheng, Z.C. Liu, Exergy destruction minimization: A principle to convective heat transfer enhancement, Int J Heat Mass Tran 122 (2018) 11–21.
[24] J. Wang, W. Liu, Z. Liu, The application of exergy destruction minimization in convective heat transfer optimization, Appl. Therm. Eng. 88 (2015) 384–390.
[25] Xiaoyue, Liu, Jensen, Michael, K., Geometry Effects on Turbulent Flow and Heat Transfer in Internally Finned Tubes, Journal of Heat Transfer, 123 (2001) 1035-1044.
[26] P. Jasinski, Numerical optimization of flow-heat ducts with helical micro-fins, using Entropy Generation Minimization (EGM) method, in: in: IASME/WSEAS international conference on fluid mechanics & aerodynamics, 2011, pp. 47–54.
[27] M. Cavazzuti, M.A. Corticelli, Optimization of heat exchanger enhanced surfaces through multiobjective genetic algorithms, Numerical Heat Transfer, Part A: Applications 54 (6) (2008) 603–624.
[28] E. Nobile, F. Pinto, G. Rizzetto, Geometric parameterization and multiobjective shape optimization of convective periodic channels, Numerical Heat Transfer, Part B: Fundamentals 50 (2006) 425–453.
[29] S. Soleimani, M. Campbel, S. Eckels, Performance analysis of different transverse and axial micro-fins in a turbulent-flow channel, Int J Therm Sci 149 (2020), 106185.
[30] P. Ranut, G. Janiga, E. Nobile, D. Thévenin, Multi-objective shape optimization of a tube bundle in cross-flow, Int J Heat Mass Tran 68 (2014) 585–598.
[31] S. Patankar, C. Liu, E. Sparrow, Fully developed flow and heat transfer in ducts having streamwise-periodic variations of cross-sectional area, 99 (1977) 180-186.
[32] A. Inc, ANSYS Fluent Theory Guide, Release 2019 (2019) R3.
[33] M. Wolfshtein, The velocity and temperature distribution in one-dimensional flow with turbulence augmentation and pressure gradient, Int J Heat Mass Tran 12 (3) (1969) 301–318.
[34] M. Spiegel, T. Redel, Y.J. Zhang, T. Struffert, J. Hornegger, R.G. Grossman, A. Doerfler, C. Karmonik, Tetrahedral vs. polyhedral mesh size evaluation on flow velocity and wall shear stress for cerebral hemodynamic simulation, Comput Methods Biomech Biomed Engin 14 (2011) 9–22.
[35] M. Sosnowski, J. Krzywanski, K. Grabowska, R. Gnatowska, Polyhedral meshing in numerical analysis of conjugate heat transfer, in: P. Dancova (Ed.) Efm17 - Experimental Fluid Mechanics 2017, E D P Sciences, Cedex A, 2018.
[36] S.M. Salim, S.C. Cheah, Wall y(+) Strategy for Dealing with Wall-bounded Turbulent Flows, in: O. Castillo, C. Douglas, D.D. Feng, J.A. Lee (Eds.) Imecs 2009: International Multi-Conference of Engineers and Computer Scientists, Vols I and Ii, Int Assoc Engineers-Iaeng, Hong Kong, 2009, pp. 2165-2170.
[37] I.B. Celik, U. Ghia, P.J. Roache, C.J. Freitas, Procedure for estimation and reporting of uncertainty due to discretization in CFD applications, J. Fluids Eng.-Trans. ASME 130 (2008) 4.
[38] A. Abdollahi, M. Shams, Optimization of heat transfer enhancement of nanofluid in a channel with winglet vortex generator, Appl. Therm. Eng. 91 (2015) 1116–1126.
[39] K. Deb, A. Pratap, S. Agarwal, T. Meyarivan, A fast and elitist multiobjective genetic algorithm: NSGA-II, IEEE Trans. Evol. Comput. 6 (2) (2002) 182–197.
[40] C.L. Hwang, K. Yoon, Methods for Multiple Attribute Decision Making, Multiple Attribute Decision Making (1981).
[41] K. Yoon, A Reconciliation Among Discrete Compromise Solutions, Journal of the Operational Research Society 38 (1987) 277–286.
[42] C.L. Hwang, Y.J. Lai, T.Y. Liu, A new approach for multiple objective decision making, Comput. Oper. Res. 20 (1993) 889–899.